Nanoscale

PAPER

View Article Online
View Journal | View Issue

Cite this: *Nanoscale*, 2024, **16**, 1758

Insights of the efficient hydrogen evolution reaction performance in bimetallic Au_4Cu_2 nanoclusters†

Aarti Devi,[a] Harpriya Minhas,[b] Lipipuspa Sahoo,[a] Rashi,[a] Saniya Gratious,[c] Amitabha Das,[b] Sukhendu Mandal,[c] Biswarup Pathak *[b] and Amitava Patra *[a,d]

The design of efficient electrocatalysts for improving hydrogen evolution reaction (HER) performance using atomically precise metal nanoclusters (NCs) is an emerging area of research. Here, we have studied the HER electrocatalytic performance of monometallic Cu_6 and Au_6 nanoclusters and bimetallic Au_4Cu_2 nanoclusters. A bimetallic Au_4Cu_2/MoS_2 composite exhibits excellent HER catalytic activity with an overpotential (η_{10}) of 155 mV *vs.* reversible hydrogen electrode observed at 10 mA cm^{-2} current density. The improved HER performance in Au_4Cu_2 is due to the increased electrochemically active surface area (ECSA), and Au_4Cu_2 NCs exhibits better stability than Cu_6 and Au_6 systems and bare MoS_2. This augmentation offers a greater number of active sites for the favorable adsorption of reaction intermediates. Furthermore, by employing X-ray photoelectron spectroscopy (XPS) and Raman analysis, the kinetics of HER in the Au_4Cu_2/MoS_2 composite were elucidated, attributing the favorable performance to better electronic interactions occurring at the interface between Au_4Cu_2 NCs and the MoS_2 substrate. Theoretical analysis reveals that the inherent catalytic enhancement in Au_4Cu_2/MoS_2 is due to favorable H atom adsorption over it and the smallest ΔG_{H^*} value. The downshift in the d-band of the Au_4Cu_2/MoS_2 composite influences the binding energy of intermediate catalytic species. This new catalyst sheds light on the structure–property relationship for improving electrocatalytic performance at the atomic level.

Received 28th October 2023,
Accepted 24th November 2023

DOI: 10.1039/d3nr05445d

rsc.li/nanoscale

Introduction

The electrochemical process is an effective way to generate green hydrogen, which is considered an excellent renewable source of energy and alternative to fossil fuels.[1–3] The major challenge has been to replace e the best-known efficient platinum (Pt) electrocatalyst by developing efficient catalysts with a lower hydrogen evolution reaction (HER) overpotential for electrocatalytic applications.[4–13] Significant attention has been given to new strategies for improving the HER performance of catalysts by controlling the charge transfer process and lowering the H adsorption and desorption energies on the catalyst surface.[14] The free energy of H adsorption at the edges of MoS_2 is considered a viable HER catalyst to replace Pt. The defect-rich ultrathin MoS_2 nanosheets (NSs) are found to be an exceptional electrocatalytic activity with a low onset overpotential.[15–17] Nonetheless, their catalytic efficacy is significantly hampered by the restricted availability of catalytically active sites, primarily caused by the tendency for restacking and insufficient vertical (*i.e.*, perpendicular to the plane) charge conductivity.[18,19] Furthermore, it has been demonstrated that enhancing the surface of MoS_2 through nanoparticle decoration is an efficient method for augmenting surface area and catalytically active sites, thus enhancing intrinsic activity.[20–22] However, the lack of atomic-level precision in the size and alloy composition of traditional nanoparticles shows the difficulties in establishing an accurate relationship between structure and properties.[14,23–25,26]

Therefore, a defined structure of a catalyst would be required to tune the catalytic property at the atomic level.[27–29] As a result, significant attention has been directed towards creating highly precise architectures and employing ligand-protected metal nanoclusters with atomic-level precision.[30–32]

[a]*Institute of Nano Science and Technology, Knowledge City, Sector 81, Mohali 14036, India*
[b]*Department of Chemistry, Indian Institute of Technology (IIT) Indore, Indore, Madhya Pradesh, 453552, India. E-mail: biswarup@iiti.ac.in*
[c]*School of Chemistry, Indian Institute of Science Education and Research Thiruvananthapuram, Thiruvananthapuram, Kerala-695551, India*
[d]*School of Materials Sciences, Indian Association for the Cultivation of Science, Jadavpur, Kolkata-700032, India. E-mail: msap@iacs.res.in; Fax: +(91)-33-2473; Tel: +(91)-33-2473-4971*

† Electronic supplementary information (ESI) available. See DOI: https://doi.org/10.1039/d3nr05445d

Metal NCs, due to their ultrasmall small sizes of nearly 2 nm with fascinating properties and atomic precision, have gained significant attention towards their applications in catalysis.[33–36] Atomically precise gold nanoclusters offer precise control over their geometric structure, electronic properties, and surface ligands, thus holding significant appeal as catalysts for electrochemical reactions due to their ultrasmall size and high surface-active sites.[37–41] Zhao *et al.* investigated the performance of Au_{25} nanoclusters on MoS_2 for the hydrogen evolution reaction, achieving an overpotential of 280 mV.[42] The study emphasizes the potential of NCs to enhance the performance of HER *via* altering the interface of Au NCs with MoS_2 NSs. Gratious *et al.* reported the enhancement of the HER activity by incorporating Au_{11} nanoclusters on MoS_2 NSs, leading to an overpotential of 292 mV, and verified the stability of the H* intermediate using computational analysis.[43] However, bimetallic nanoclusters could potentially offer improved catalytic activity and selectivity compared to their monometallic nanoclusters due to the synergistic effects of heteroatoms.[44] A few investigations have explored the use of doped Au NCs with various dopants, including noble metals Pt, Pd, Ru, and Ag.[39,45] A few studies have been reported on the doping of precious materials Pd and Pt into atomically precise Au_{25} and Au_{26} NCs.[46] Zhu *et al.* investigated Au_2Pd_6 NCs over MoS_2 showing significantly improved HER catalytic activity and achieved an overpotential of nearly 225 mV *vs.* RHE at a current density of 10 mA cm^{-2}.[45] Tang *et al.* compared the HER performance of two types of bimetallic $Au_{24}Ag_{20}$ and $Au_{22}Ag_{20}$ NCs protected by alkynyl and halogen groups with overpotentials of 260 mV and 335 mV, respectively.[47] Further, DFT reveals the enhancement in HER activity based on the lower binding energy of hydrogen to form an H* intermediate. However, the dopant including non-noble metals Cu with Au NCs for electrocatalytic HER performance has limited exploration.

Here, we synthesized atomically precise bimetallic Au_4Cu_2 NCs and monometallic Au_6 and Cu_6 NCs for hydrogen evolution reaction (HER) catalytic activity. A comprehensive analysis involving experimental and theoretical approaches provides valuable insights into the mechanistic aspects responsible for the improved HER catalytic activity observed in the bimetallic Au_4Cu_2/MoS_2 composite. XPS studies confirm better charge transfer between Au_4Cu_2 NCs and MoS_2, indicating strong electronic interactions at their interface. Theoretical analysis reveals that the intrinsic catalytic improvement in the Au_4Cu_2/MoS_2 composite is due to its favorable H atom adsorption and the smallest ΔG_{H^*} value.

Experimental details

Materials

Sodium molybdate dihydrate ($Na_2MoO_4{\cdot}2H_2O$, 99.99%), thiourea (CH_4N_2S, 99%), tetrachloroauric acid trihydrate ($HAuCl_4{\cdot}3H_2O$), copper nitrate trihydrate ($Cu(NO_3)_2{\cdot}3H_2O$), tetrakis(hydroxymethyl)phosphonium chloride (THPC), 3-mercaptopropionic acid (MPA), sodium hydroxide (NaOH), Nafion (5 wt% in low aliphatic alcohols), Pt/C (20 wt% Pt loading on Vulcan XC-72) were obtained from Sigma-Aldrich. Sulfuric acid (H_2SO_4, 98%) was purchased from Thermo-Fisher Scientific India Ltd. All the chemicals were purchased in ultrapure form; therefore, no additional purification was required. The glassware was thoroughly cleaned with aqua regia and rinsed with ultrapure water and acetone before use.

Characterization

Scanning electron microscopy (SEM) images were obtained using a JEOL, JSMIT-300. Transmission electron microscopy (TEM) and high-resolution TEM images were taken using a JEOL-JEM-F200 instrument. Powder X-ray diffraction (PXRD) patterns were analyzed on a Bruker D8 ADVANCE powder diffractometer with Cu Kα radiation. Raman spectra were recorded in a WITEC Focus Innovations Alpha-300 Raman confocal microscope using a 532 nm excitation laser. XPS measurements were recorded using a Thermo-Fischer Scientific Kα instrument. Waters Q-TOF mass spectrometer equipped with a Z-spray source was used for the electrospray ionization (ESI) mass spectrometry measurements. The mass of as-synthesized NCs was examined using matrix-assisted laser desorption ionization-time of flight (MALDI-TOF) mass spectrometry on a Bruker Daltonics Autoflex II TOF/TOF system. Ultraviolet–Visible (UV-Vis) absorption spectra were collected from a UV-Vis spectrophotometer (Shimadzu). Fourier-transform infrared (FTIR) spectra were performed in a PerkinElmer FTIR-spectrometer using KBr pellets. The PL spectra were recorded using a Fluorolog 3-221 (HORIBA Jobin Yvon) fluorimeter. Inductively coupled plasma mass spectrometry (ICP-MS) analysis was performed using an Agilent 7900 instrument.

Synthesis of monometallic copper and gold nanoclusters

The synthesis of Cu NCs involves a one-pot strategy. In a beaker, 10 mL of high performance liquid chromatography (HPLC) water was mixed with 75 mL of 1 M NaOH and 3 μL of THPC (80% in water), with vigorous stirring. Then, 100 μL of copper salt was added, resulting in a color change to light brown, indicating the reduction of copper salt. After 30 minutes of stirring, an MPA ligand was introduced, and the reaction continued under stirring in the dark at room temperature. The change in the reaction mixture's color after 24 hours confirmed the formation of MPA-capped gold NCs. The synthesis of gold nanoclusters follows the same one-pot strategy by taking gold salt as a metal precursor in the case of Au NCs.

Synthesis of bimetallic copper doped gold nanoclusters

The synthesis of copper-doped gold nanoclusters was previously reported with the same methodology as for Au_6 NCs with minor modifications. In a one-pot synthesis, two metal precursors (Au^{3+} and Cu^{2+}) with a $[Cu^{2+}]/[Au^{3+}]$ ratio of 0.047 were analyzed using ICP-MS. The as-synthesized Cu_6, Au_6, and Au_4Cu_2 NCs were washed multiple times with HPLC water to

eliminate excess ligands and centrifuged at 14 000 rpm for further analysis.

Synthesis of MoS_2 NSs

The synthesis involves previously reported procedures. Initially, 800 mg of $Na_2MoO_4{\cdot}2H_2O$ was dissolved in 10 mL of distilled water with magnetic stirring to prepare 2D MoS_2 NSs. Separately, 1.65 mg of thiourea was mixed with 16.6 mL of distilled water. The colorless thiourea solution was slowly added to $Na_2MoO_4{\cdot}2H_2O$ solution until it became clear. The mixture was then placed in a Teflon-lined stainless-steel autoclave and heated at 200 °C for 24 hours. After cooling to room temperature, black residues were obtained by centrifuging the solution at 12 000 rpm for 30 minutes. These residues were washed with HPLC water and ethanol and dried at 60 °C in an air oven for further analysis.

Preparation of Cu_6 NCs, Au_6 NCs and Au_4Cu_2 NCs composites with MoS_2 NSs

Initially, 2 mg of MoS_2 was mixed well with 0.35 mL of water through ultrasonication for 10 min. After that, different amounts of Cu_6 NCs, Au_6 NCs, and Au_4Cu_2 NCs were added into the above-dispersed mixture and were allowed to sonicate for 30 min for better interaction between as-prepared NCs and MoS_2. The composites were then separated using centrifugation to confirm the successful loading of each type of NCs on MoS_2, and the ICP-MS technique analyzed the loading of NCs present in a given system.

Preparation of working electrode for HER

Typically, 2 mg of MoS_2 NSs was suspended in a solution containing a mixture of ethanol, water, and Nafion (in a ratio of 1 : 4 : 0.55) and sonicated to produce a well-dispersed suspension. Thereafter, 150 μL of NCs solution was added and sonicated for 30 minutes to obtain a homogeneous ink. 5 μL of ink was drop-casted onto a 3 mm diameter glassy carbon rotating disk electrode followed by drying under an IR lamp for 5 hours. The NCs loading on MoS_2 NSs was regulated by varying the amount of NCs in the dispersion of MoS_2 NSs. Similarly, a working electrode for bare MoS_2 NSs was prepared without NCs. The working electrode of commercial Pt/C was fabricated by 50 μg cm^{-2} Pt loading on the electrode surface.

Electrochemical measurements

All electrochemical measurements were recorded using an Autolab multichannel M204 PGSTAT (Metrohm) electrochemical station by taking 0.5 M H_2SO_4 aqueous solution at 25 °C. A conventional three-electrode system was used to assess the performance of the HER. The working electrode was a catalyst-coated glassy carbon RDE, a graphite rod served as a counter electrode, and the reference electrode was a saturated calomel electrode (SCE). The formula ERHE = ESCE + (0.241 + 0.059 pH) was used to convert all the potential values in the study to the reversible hydrogen electrode (RHE) scale. HER linear sweep voltammetry (LSV) curves were obtained at a scan rate of 10 mV s^{-1}. To calculate the double-layer capacitance, cyclic voltammograms with scan rates ranging from 10 to 50 mV s^{-1} were acquired in the non-faradaic potential ranging from 0.0 to 0.3 V *vs.* RHE (C_{dl}). The double-layer capacitance was determined by plotting the difference between the anodic and cathodic currents ($\Delta J = J_a - J_c$) at 0.15 V *vs.* RHE as a function of scan rate.[48] The C_{dl} was measured using the formula:

$$C_{dl} = \frac{d(\Delta J)}{2dV} \quad (1)$$

The electrochemically active surface area (ECSA) can be obtained by using the measured C_{dl} values of the samples, from the formula: ECSA = C_{dl}/C_s, where C_s indicates the specific capacitance of the flat standard electrode, *i.e.*, C_s = 0.04 mF Cm^{-2}.[49] The electrochemical impedance spectra in the 100 kHz to 0.1 Hz frequency range were determined using an AC voltage having 10 mV amplitude. The measured impedance spectra were then fitted into an appropriate equivalent circuit model to ascertain the solution resistance and charge transfer resistance. A long-term durability test was done by collecting a chronoamperometric curve for 40 hours at a constant potential to attain a current density of 10 mA cm^{-2} at 25 °C. All the data are reported without iR-correction.

Computational details

The density functional theory (DFT) calculations were performed using the projected augmented wave (PAW) method implemented in the Vienna *ab initio* simulation package (VASP).[50,51] The generalized gradient approximation with Perdew–Burke–Ernzerhof (GGA-PBE) was employed to describe the exchange–correlation functionals.[52] Plane-wave basis sets were set at 550 eV to expand the electronic wave function. A Γ-centre (1 × 1 × 1) *k*-points grid was considered for sampling the Brillouin zone. A conjugate-gradient algorithm with an energy convergence criterion of 10^{-4} eV and Hellmann–Feynman force convergence criteria of <0.02 eV $Å^{-1}$ was utilized during optimization. The DFT-D3 method was used to take into account the van der Waals interaction.[52] The reaction free energies (ΔG) were calculated by considering the following equation:[53,54]

$$G = \Delta E + \Delta E_{ZPE} - T\Delta S \quad (2)$$

where ΔE is the hydrogen binding energy, ΔE_{ZPE} is the change in zero-point energy, T is the temperature (300K), and ΔS is the entropy change for the reaction. ΔE_{ZPE} and entropies were calculated from the harmonic oscillator approximation.[55] The zero-point energy (E_{ZPE}) was calculated using the following equation:

$$E_{ZPE} = \sum \frac{1}{2} h\nu \quad (3)$$

where h is the Planck constant and ν is the vibrational frequency.

Results and discussion

We have synthesized Au_6 NCs, Cu_6 NCs, and Au_4Cu_2 NCs utilizing a one-pot synthesis method in an aqueous medium with MPA as a capping ligand.[56] The TEM images of as-prepared Cu_6 NCs and Au_6 NCs depict the formation of ultrasmall nanoclusters with spherical morphology and an acquired particle size distribution indicating a size of nearly 2 nm (Fig. S1†). The recorded TEM and HRTEM images of bimetallic Au_4Cu_2 NCs also depict the formation of ultrasmall nanoclusters with an average size of 2.03 ± 0.3 nm (Fig. S2a and b†). The elemental mapping by TEM of bimetallic Au_4Cu_2 NCs shows clear evidence of the presence of both Au and Cu in the prepared bimetallic NCs (Fig. S2c–f†). In-depth analysis through positive-mode ESI-mass spectrometry provided insights into the composition of the synthesized NCs. For the as-prepared Cu NCs, a prominent peak at *m*/*z* 903 Da corresponds to $[Cu_6(MPA)_5 + H^+]^+$, while for the Au_6 NCs, the molecular ion peak observed at 1754 Da is attributed to $[Au_6(MPA)_5 + 2Na^+ - H^+]^+$ (Fig. 1a and b). The additional peaks in mass spectrometry are attributed to the loss of fragments from the molecular ion.[57] Notably, an additional peak at a separation of *m*/*z* 146 (marked with an asterisk) in the case of Au NCs is due to $[Au_6(MPA)_4 + H^+]^+$, suggesting the detachment of an MPA ligand fragment from $Au_6(MPA)_5$. This interpretation is supported by a close match between the isotopic experimental pattern and the simulated pattern, as depicted in Fig. S3.† Furthermore, in the case of the bimetallic AuCu NCs, the observed *m*/*z* peak at 1552 Da corresponds to the composition $[Au_4Cu_2(MPA)_5 + 5Na^+ - 4H^+]^+$ (Fig. 1c). Thus, the inclusion of Cu in Au NCs results in the replacement of a few Au atoms by Cu atoms. The assigned compositions in all as-prepared NCs are substantiated by the close match between the isotope distributions of the simulated and observed spectra, as seen in Fig. 1(i, ii, iii). The composition of as-prepared NCs was further confirmed with MALDI-MS analysis (Fig. S4†). The MALDI-MS analysis of Au NCs exhibits a molecular ion peak at *m*/*z* 1729 Da attributed to $[Au_6(MPA)_5 + Na^+]$, and other peaks at (a) *m*/*z* 1497 Da and (b) *m*/*z* 1207 Da can be assigned to $[Au_6(MPA)_3 + H^+]$ and $[Au_4(MPA)_4 + H^+]$, respectively, arising from the decomposition of $(MPA)_2$ and $Au_2(MPA)$ fragments from $Au_6(MPA)_5$. Further, the MALDI-MS analysis of AuCu NCs includes a molecular ion peak at *m*/*z* 1507 Da that can be attributed to $[Au_4Cu_2(MPA)_5 + 3Na^+]$, and other peaks at (a) *m*/*z* 1297 Da and (b) *m*/*z* 1073 Da can be assigned to $[Au_4Cu_2(MPA)_3 + 3Na^+]$ and $[Au_4Cu_2(MPA)_2 + H^+]$, respectively, arising from the fragmentation of $(MPA)_2$ and $(MPA)_3$ ligands from $Au_4Cu_2(MPA)_5$. Investigation into the ligand binding characteristics of the NCs was conducted using FTIR spectra analysis (Fig. S5†). In the FTIR spectra of the MPA ligand, a peak is evident at 2567 cm^{-1}, representing the S–H thiol group. However, upon the formation of as-prepared Cu_6 NCs, Au_6 NCs, and Au_4Cu_2 NCs, this peak disappears, providing evidence for the formation of covalent Au–S and Cu–S bonds in the NCs. The as-prepared NCs exhibit tunability in photophysical properties. The UV-Vis absorption spectra of the as-prepared NCs exhibit no SPR bands at 520 nm or 650 nm due to Au NPs or Cu NPs, suggesting no formation of nanoparticles.[58,59] Interestingly, the UV-Vis absorption spectra of Cu_6 NCs, Au_6 NCs, and Au_4Cu_2 NCs exhibit prominent differences, as seen in Fig. 1d. The absorption peaks for monometallic Cu_6 NCs and Au_6 NCs were observed at 346 nm and 380 nm. After the inclusion of copper in Au_6 NCs, the UV-Vis peak red-shifted to 420 nm in the case of Au_4Cu_2 NCs, revealing perturbation in the electronic structure of the Au_6 NCs after Cu substitution. Similarly, the prepared NCs exhibit different photoluminescence (PL) properties. The Cu_6 NCs are non-luminescent while Au_6 NCs exhibit an emission peak at 520 nm which is red-shifted to 620 nm in the case of Au_4Cu_2 NCs, due to the tunability of the HOMO–LUMO gap after the inclusion of Cu atoms in Au NCs.[56] Moreover, the recorded

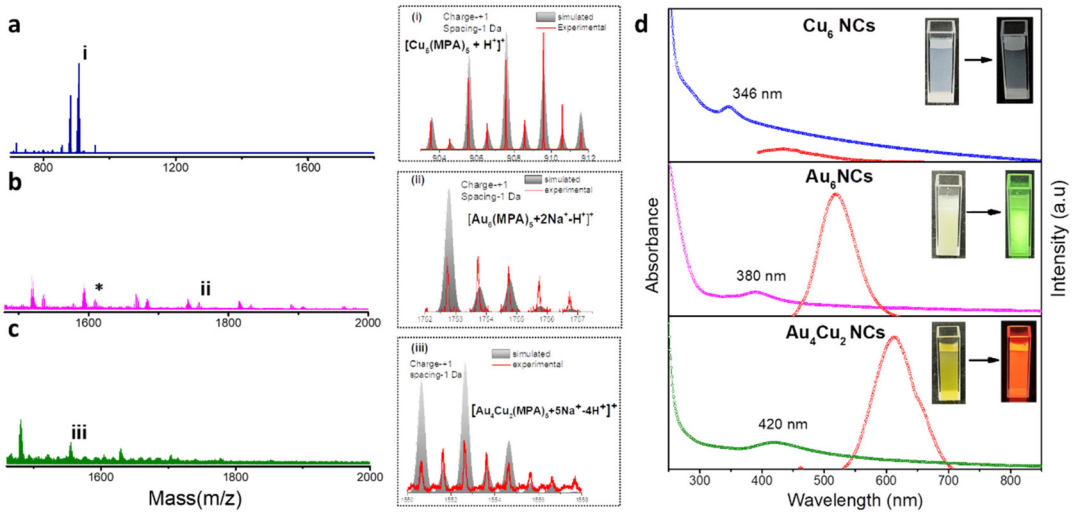

Fig. 1 ESI-mass spectra and corresponding isotopic patterns of (a) Cu_6 NCs, (b)Au_6 NCs, and (c) Au_4Cu_2NCs. (d) The corresponding UV-vis absorption and photoluminescence spectra. (Insets show the color of the NCs under visible and UV-light (λ_{ex} = −365 nm).).

excitation spectra of as-prepared NCs can be seen in Fig. S6.† To explore the potential of as-prepared NCs in enhancing the electrocatalytic HER, we loaded them on MoS_2, as seen in Fig. 2a. The MoS_2 NSs were prepared by a previously reported strategy.[60] The observed PXRD pattern of MoS_2 exhibits distinctive peaks corresponding to planes (002), (100), (103), and (110), closely matching the MoS_2 hexagonal structure (Fig. S7†).[60]

The Au_4Cu_2 NCs/MoS_2 composites were obtained by mixing as-prepared Au_4Cu_2 NCs in well-dispersed MoS_2 NSs in an aqueous medium followed by 30 minutes of ultrasonication. To study the formation of Au_4Cu_2NCs/MoS_2, further characterizations were performed involving SEM, TEM, and HRTEM. The SEM image of MoS_2 clearly shows the sheet-like morphology, which is entangled to form a two-dimensional sheet-like configuration with many edges and corners (Fig. 2b). Further, the elemental mapping confirms the uniform distribution of Mo and S in MoS_2 (Fig. S8†). The TEM images confirm the development of a sheet-like structure, aligning with the SEM analysis (Fig. S9†). Moreover, HRTEM images exhibit discernible lattice-fringes with spacings of 0.63 nm corresponding to the (002) plane of the MoS_2 structure (Fig. 2c). Noticeably, TEM images of the composite reveal that the MoS_2 surface is decorated by spherical Au_4Cu_2 NCs, and the NCs are uniformly encapsulated on the surface of MoS_2 NSs (Fig. 2d–e†). The obtained EDX spectrum and elemental mapping confirm the presence and uniform distribution of Mo, S, Au, and Cu in the Au_4Cu_2/MoS_2 heterostructure (Fig. S10,† Fig. 2f–j). The EDX spectrum quantifies the atomic ratio of Au/Cu of nearly 1.78, which is almost the same as that in Au_4Cu_2 NCs (inset to Fig. S10†). Thereafter, the TEM images of the Au_6/MoS_2 and Cu_6/MoS_2 composites show encapsulated NCs on the MoS_2 NSs. Additionally, the elemental mapping suggests the presence of the considered NCs on MoS_2 NSs (Fig. S11–12†).

We carried out XPS and Raman investigations to look into the interactions between NCs and MoS_2 NSs and study the inherent causes of the improvement in catalytic activity. The XPS survey spectra recorded for all considered catalysts can be seen in Fig. S13.† The Mo 3d XPS spectra of MoS_2, Cu_6/MoS_2, Au_6/MoS_2, and Au_4Cu_2 /MoS_2 are given in Fig. 3a. The peaks that appeared at 228.6 eV and 231.8 eV can be attributed to Mo $3d_{5/2}$ and Mo $3d_{3/2}$, respectively. Interestingly, Mo 3d in Au_4Cu_2/MoS_2 nanocomposites shows a larger negative shift of 0.6 eV in binding energy (B.E) than that in Au_6 NCs/MoS_2 (0.3 eV) or Cu_6 NCs/MoS_2 (0.3 eV), in comparison with pristine MoS_2, indicating better electronic interactions in case of bi-metallic Au_4Cu_2NCs with MoS_2. Similarly pronounced negative shifts (0.4 eV) are seen in the binding energies of S 2p in Au_4Cu_2/MoS_2 compared to the other considered systems or

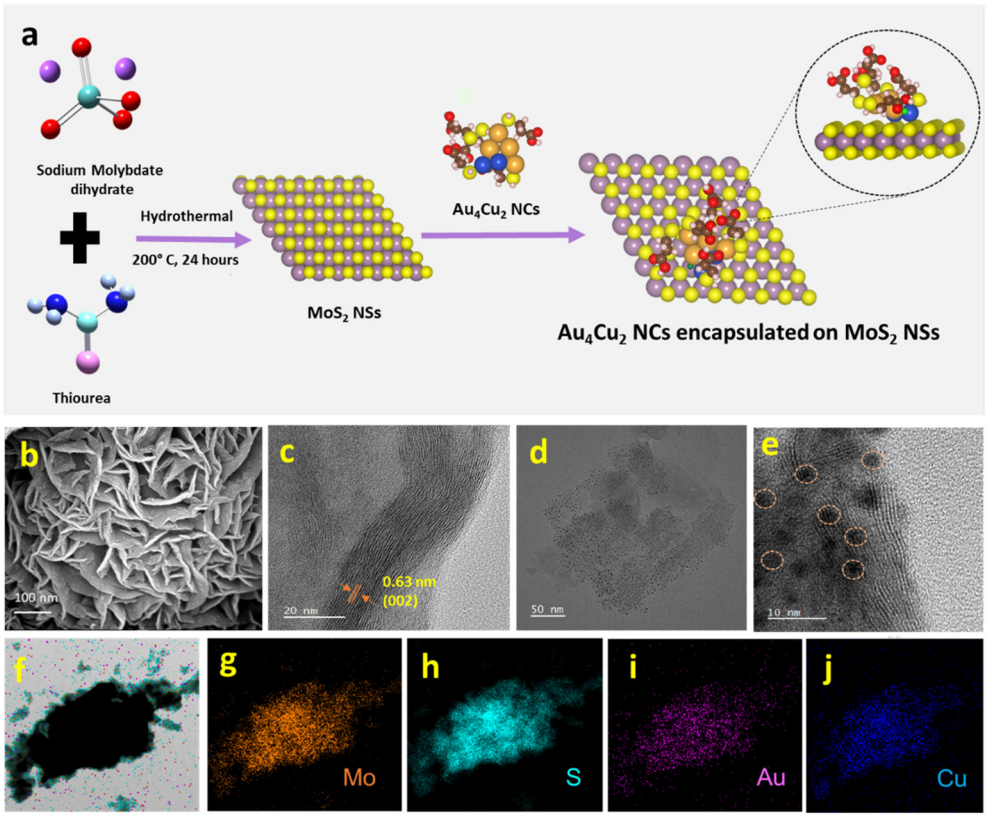

Fig. 2 (a) Schematic illustration of the synthesis of MoS_2 and Au_4Cu_2/MoS_2 heterostructures. (b) SEM and (c) HRTEM image of MoS_2 NSs. (d) and (e) TEM and HRTEM images of Au_4Cu_2/MoS_2. (f) STEM image of Au_4Cu_2/MoS_2 with the corresponding elemental mappings of (g) Mo, (h) S, (i) Au, and (j) Cu.

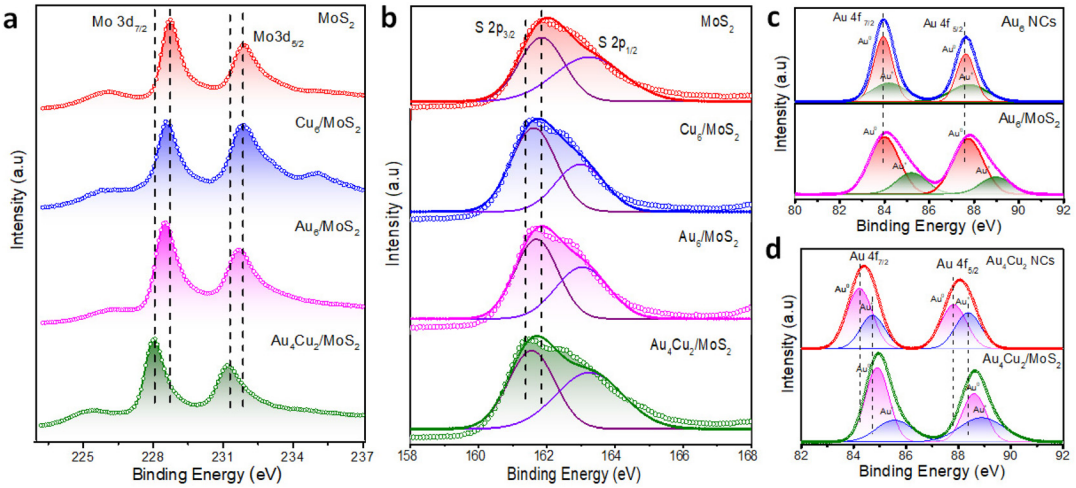

Fig. 3 XPS analysis of MoS_2, Cu_6/MoS_2, Au_6/MoS_2, and Au_4Cu_2NCs/MoS_2: (a) Mo 3d, (b) S 2p, (c) XPS spectra of Au 4f in Au_6 NCs and Au_6/MoS_2, and (d) XPS spectra of Au 4f in Au_4Cu_2 NCs and Au_4Cu_2/MoS_2.

bare MoS_2 (Fig. 3b). Au 4f exhibits twin peaks between 80 and 90 eV for all considered catalysts, corresponding to Au $4f_{7/2}$ and Au $4f_{5/2}$.[61] Further analysis involved the splitting of these two peaks revealing the presence of both Au(0) and Au(I) valence states, and these mixed oxidation states were well-matched with previous findings.[62] Interestingly, the (B.E) of Au 4f in Au_6NCs and Au_4Cu_2NCs shows positive shifts of 0.3 eV and 0.6 eV, respectively, with their heterostructures compared to bare Au_6NCs and Au_4Cu_2NCs, which corroborates the effect of deposited NCs on the electronic properties of MoS_2 (Fig. 3c–d). A similar kind of positive shift of 0.2 eV was observed in the Cu 2p of the pure nanocluster compared to its Cu_6/MoS_2 composite (Fig. S14†).[63] These findings imply the considerable transfer of electron density between deposited NCs and the MoS_2 interface. The Raman spectrum corresponding to MoS_2 can be seen in Fig. S15.† The Raman peaks at 378 cm^{-1} and 405 cm^{-1} correspond to typical $E_{2g}{}^1$ and $A_{1g}{}^1$ vibration modes, respectively.[64] Here the creation of multilayered MoS_2 is indicated by the frequency difference ($\Delta k \sim 27$ cm^{-1}) between the phonon modes, $E_{2g}{}^1$ and $A_{1g}{}^1$. However, after Au_4Cu_2 NCs were encapsulated on MoS_2, the in-plane $E_{2g}{}^1$ vibration frequency mode was shifted towards a higher wavenumber due to structural changes brought on by stacking or interfacial van der Waals interactions due to substantial electron density transfer between Au_4Cu_2 NCs and MoS_2 NSs.

Electrocatalytic water reduction performance

The electrocatalytic HER activity of bare MoS_2 and considered nanocomposites was analyzed using a typical three-electrode system taking 0.5 M H_2SO_4 as an electrolyte. Commercial Pt/C was used as a benchmark catalyst using a metal loading of 50 μg cm^{-2} on the glassy carbon electrode. Pt/C displays the lowest overpotential of 13 mV *vs.* RHE (reversible hydrogen electrode) and a very high current density of nearly 500 mA cm^{-2} at a comparatively low overpotential, both of which highlight the catalyst's exceptional performance (Fig. S16†). Bare MoS_2 shows a current density of 55 mA cm^{-2} at a potential of −0.4 V (Fig. 4a). The HER catalytic performance was found to depend on the different concentrations of NCs. For comparison, we investigated the best HER catalytic activity of all considered catalysts, such as Cu_6/MoS_2, Au_6/MoS_2, and Au_4Cu_2/MoS_2, by taking different loading amounts of as-prepared NCs on the base material MoS_2 (Fig. S17a–c†). The compared HER polarization curves show that the best HER activity is exhibited by a 2 wt% Au_4Cu_2/MoS_2 nanocomposite, whereas the activity of 3 wt% Au_6/MoS_2 and 2 wt% Cu_6/MoS_2 composites is comparable to that of MoS_2. Au_4Cu_2/MoS_2 exhibits a prominent activity of 130 mA cm^{-2} which is 1.41, 1.91, and 2.36 times higher than that of Au_6/MoS_2, Cu_6/MoS_2, and bare MoS_2, respectively (Fig. 4a). This implies that introducing Cu dopant into Au NCs can significantly enhance electrocatalytic performance. Fig. S18† emphasizes the charge transport region, wherein the current is governed by the rate of charge transfer at the electrode surface. Herein, the Au_4Cu_2/MoS_2 catalyst shows an overpotential of 155 mV at a current density of 10 mA cm^{-2}, which is notably lower than that of the other considered catalysts or bare MoS_2 (Fig. 4b). Furthermore, other HER electrocatalytic factors, such as Tafel slope, charge-transfer resistance, and electric double-layer capacitance, were examined by varying the loading amounts of Au_4Cu_2 NCs on MoS_2. The findings also indicate the most favorable outcomes with a loading of 2 wt% Au_4Cu_2 NCs on MoS_2 (Fig. S19a–c†). The double-layer capacitance corresponding to variable loadings of Au_4Cu_2/MoS_2 was analyzed by recording cyclic voltammograms at various scan rates (Fig. S20a–e†). The overall electrocatalytic parameters for Au_4Cu_2/MoS_2 are tabulated in Table S1.† After that, to better comprehend the considered systems, Tafel slope analysis of various considered catalysts was used to determine the rate of electron transport at the electrode–electrolyte interface, as shown in Fig. 4c, of MoS_2, Cu_6/MoS_2, Au_6/MoS_2, Au_4Cu_2/MoS_2, and commercial Pt/C, created from the HER polarization curves. Commercial Pt/C

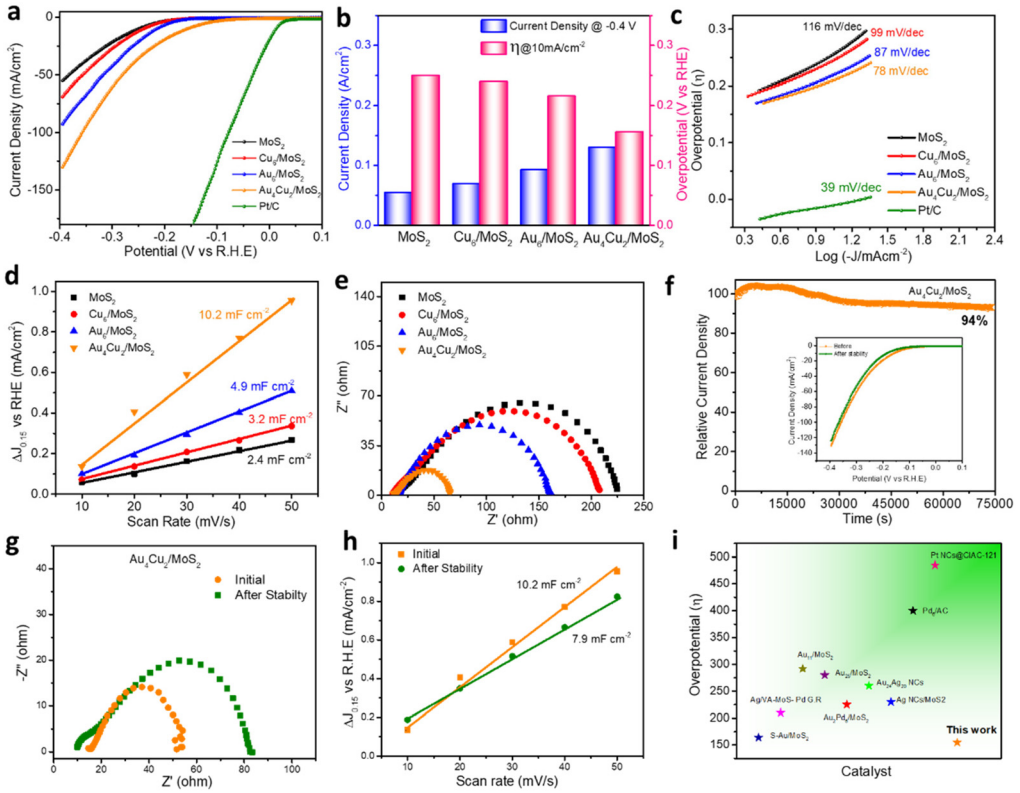

Fig. 4 (a) Polarization curves of MoS_2, NC-encapsulated MoS_2, and Pt/C towards HER recorded at a scan rate of 10 mV s^{-1}. (b) comparison of the current density at −0.4 V *vs.* RHE (blue columns) and overpotential at a current density of 10 mA cm^{-2} (pink columns). (c) Corresponding Tafel slopes obtained from the low-current density region. (d) Corresponding C_{dl} plot. (e) Nyquist plots of various catalysts. (f) Chronoamperometry plot of Au_4Cu_2/MoS_2 (inset shows the HER polarization curve before and after catalysis). (g) Nyquist plot and (h) relative C_{dl} plot as a function of scan rate for Au_4Cu_2/MoS_2 before and after catalysis. (i) Overpotential at a current density of 10 mA cm^{-2} of Au_4Cu_2/MoS_2 in comparison with the overpotential of previously reported catalysts.

exhibits the lowest Tafel slope of 39 mV dec^{-1}, as reported in the literature.[65] Furthermore, the Tafel slope of Au_4Cu_2/MoS_2 is much smaller in comparison to the other considered catalysts, as seen in Fig. 4c. The Tafel slope obtained for the Au_4Cu_2/MoS_2 bimetallic composite is 78 mV dec^{-1}, which is considerably less than for the other considered catalysts Cu_6/MoS_2 (97 mV dec^{-1}), Au_6/MoS_2 (87 mV dec^{-1}), and bare MoS_2 (116 mV dec^{-1}), indicating greater enhancement in the HER kinetics of MoS_2 in the presence of Au_4Cu_2 NCs. Moreover, the measured Tafel slope of 78 mV dec^{-1} for Au_4Cu_2/MoS_2 suggests that HER may occur *via* a coupled Volmer–Heyrovsky-type mechanism, with the electrochemical adsorption–desorption process serving as the rate-limiting step.[66] Further in-depth investigation of the electrochemically active surface area (ECSA) and charge transfer properties helped to clarify the cause of the increased electrocatalytic activity for Au_4Cu_2/MoS_2 heterostructures. ECSA is also crucial because it influences the rate at which charge transfer reactions occur at the electrode–electrolyte interface. Fig. 4d shows a comparison plot of double layer capacitance (C_{dl}) as a function of scan rate. The C_{dl}, which directly affects the ECSA, was calculated using the cyclic voltammograms of MoS_2 and other considered catalysts at various scan rates, as shown in Fig. S21.†[67] The calculated C_{dl} for the Au_4Cu_2/MoS_2 heterostructure is 10.2 mF cm^{-2}, which is 2.0, 3.1, and 4.2 times higher than the estimated C_{dl} for Au_6/MoS_2, Cu_6/MoS_2, and bare MoS_2. This suggests that the former has more active sites and ECSA due to the creation of an interfacial structure. The charge transfer kinetics at the electrode surface during the HER process were investigated using electrochemical impedance spectroscopy (EIS). The charge transfer process is represented by a semicircle at high frequencies, and the diameter of the semicircle equals the charge transfer resistance (R_{ct}).[68,69] The Nyquist curve presented in the inset of Fig. 4e shows faster charge transfer kinetics of the Au_4Cu_2/MoS_2 composite as it exhibits the smallest diameter for the semicircle in comparison to the other catalysts and bare MoS_2, due to the synergistic interaction between Au_4Cu_2 NCs and MoS_2. This indicates a rapid electron transfer rate at the catalyst–electrolyte interface, leading to remarkable hydrogen evolution activity. The electrochemical performance of all the catalysts is shown in Table 1. Long-term durability is a crucial consideration when evaluating an electrocatalyst for improving catalytic performance. To examine the stability of the electrocatalyst, chronoamperometry measurements of MoS_2, Cu_6/MoS_2, Au_6/MoS_2, and Au_4Cu_2/MoS_2 were performed at a fixed potential to achieve an initial current density of

Table 1 Summary of HER overpotential, Tafel slope, double-layer capacitance, electrochemically active surface area, and charge-transfer resistance of MoS_2, Cu_6/MoS_2, Au_6/MoS_2, Au_4Cu_2/MoS_2, and commercial Pt/C

Catalyst	Overpotential at 10 mA cm^{-2} (mV *vs.* RHE)	Tafel slope (mV dec^{-1})	Double-layer capacitance C_{dl} (mF cm^{-2})	Electrochemically active surface area ECSA (cm^2)	Charge-transfer resistance R_{ct} (Ohm)
MoS_2	252	116	2.4	60	210
Cu_6/MoS_2	240	99	3.2	80	197
Au_6/MoS_2	215	87	4.9	123	162
Au_4Cu_2/MoS_2	155	78	10.2	255	39
Pt/C	13	39	—	—	—

10 mA cm^{-2}. The Cu_6/MoS_2 and Au_6/MoS_2 composites demonstrate initial current density stabilities of 55% and 60%, respectively, indicating slightly improved stability compared to bare MoS_2 (52%) (Fig. S22†). However, the Au_4Cu_2/MoS_2 composite shows better stability by maintaining nearly 94% of its initial current density even after 75 000 seconds of stability testing. The inset of Fig. 4f shows the HER catalytic activity acquired before and after the chronoamperometry testing of Au_4Cu_2/MoS_2, which demonstrates an increase in η_{10} of only 17 mV and a decrease in current density of 7 mA cm^{-2} after the stability test.

Bare MoS_2 shows a greater increase in η_{10} by 47 mV and a decrease in current density of nearly 2 times (Fig. S23a and b†). Moreover, the recorded EIS spectra before and after the durability test depict a greater increase in charge transfer resistance for bare MoS_2 NSs in comparison to Au_4Cu_2/MoS_2 (Fig. 4g). The C_{dl} of Au_4Cu_2/MoS_2 is still three times greater than the original C_{dl} value of MoS_2, indicating that the active sites are intact even after catalysis (Fig. 4h, Fig. S24†). We evaluated the stability of Au_4Cu_2/MoS_2 by analyzing LSV for 2000 cycles at a scan rate of 50 mV s^{-1} to assess the change in overpotential at a constant current density. After the LSV cycling stability test, there is a decrease in overpotential by 9 mV at 10 mA cm^{-2} current density, which reveals the excellent stability of Au_4Cu_2/MoS_2 (Fig. S25†). The findings imply that the loading of Au_4Cu_2 NCs enhances the stability of MoS_2 by protecting the catalytically active sites during catalysis as a result of the robust electronic interactions between the two materials. There is no doubt that these results are better than previous findings so far (Fig. 4i and Table S2†). The nanosheet morphology of the catalyst (Au_4Cu_2/MoS_2) remains unscratched after the stability test, as seen from its recorded TEM images (Fig. S26†).

Theoretical approach

As we do not have the crystal structures of the nanoclusters, we modelled these clusters by considering a neutral ligand based on previous experimental and theoretical reports.[56,70] We also followed a previous theoretical report where MPA is considered as a neutral ligand and the calculated results were very much in agreement with the experimental trend.[56] On the other hand, the number of possible arrangements would be very large if we considered the possible oxidation states of the metal. Therefore, we modelled the clusters by considering the neutral ligand. DFT calculations were carried out to unveil the influence of pristine MoS_2, $Au_6(MPA)_5/MoS_2$, $Cu_6(MPA)_5/MoS_2$, and $Au_4Cu_2(MPA)_5/MoS_2$ clusters on the HER. To mimic the experimentally synthesized cluster on an MoS_2 support, initial optimization was performed for the $Au_6(MPA)_5$ and $Cu_6(MPA)_5$ clusters.[55] In the $Au_6(MPA)_5$ cluster, two Au atoms were replaced with Cu atoms in all possible positions (A12, A13, A14, and A13′), as shown in Fig. S27.† Subsequently, $Au_6(MPA)_5$, $Cu_6(MPA)_5$, and $Au_4Cu_2(MPA)_5$ clusters were deposited onto the MoS_2 support, considering various possible orientations (Fig. S28–S30†). The final configuration with the most stable positions is shown in Fig. 5A.

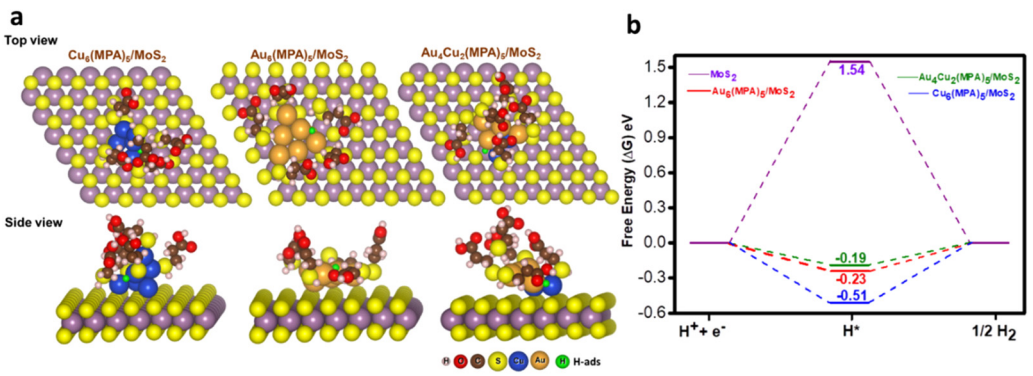

Fig. 5 (a) The top and side views of the most stable H-adsorption sites on the most stable orientation of clusters on the MoS_2 support: $Cu_6(MPA)_5/MoS_2$, $Au_6(MPA)_5/MoS_2$, and $Au_4Cu_2(MPA)_5/MoS_2$. (b) Free energy diagrams of pristine MoS_2, $Cu_6(MPA)_5/MoS_2$, $Au_6(MPA)_5/MoS_2$, and $Au_4Cu_2(MPA)_5/MoS_2$ for HER.

Here, all the possible sites in all the clusters deposited on the MoS_2 surface for H adsorption are considered, as shown in Fig. 5a and Fig. S31–S34.† The Au–Au bridge, Cu–Cu bridge, Au–Cu bridge, on top of Au and top of S are found to be the most stable sites for H adsorption on $Au_6(MPA)_5/MoS_2$, $Cu_6(MPA)_5/MoS_2$, $Au_4Cu_2(MPA)_5/MoS_2$ and pristine MoS_2 surface, respectively. It is the cooperative effect of Au–Cu that helped the better adsorption of H on the most active

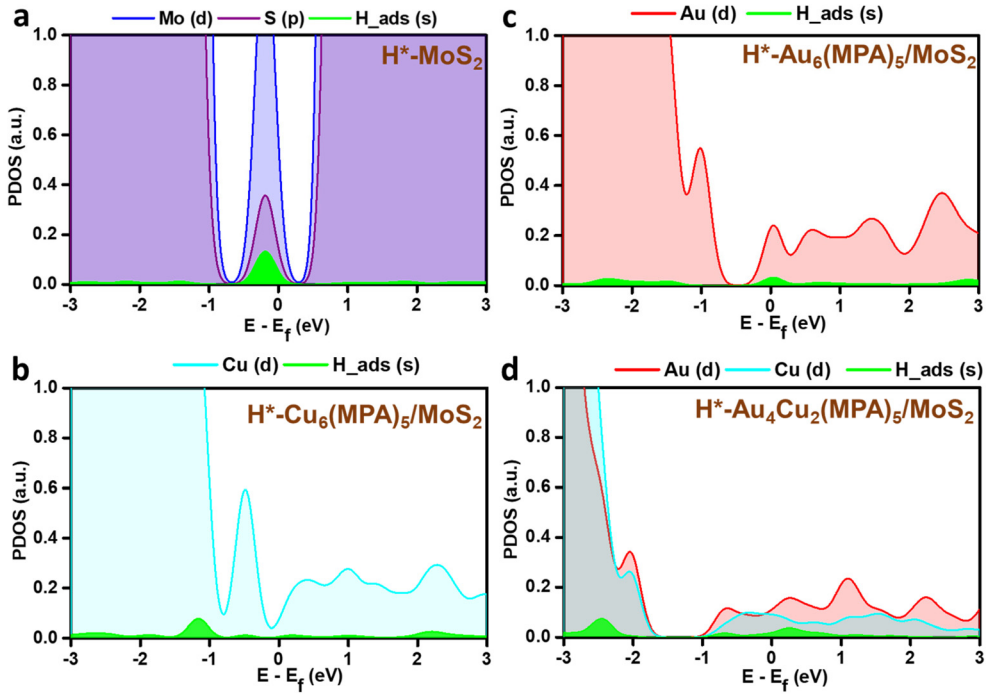

Fig. 6 Partial density of states (PDOS) of the 1s orbital of H in green and 4d orbitals of (a) Mo (blue) and S (purple), (b) Cu (cyan), (c) Au (red), and (d) Au and Cu after H adsorption.

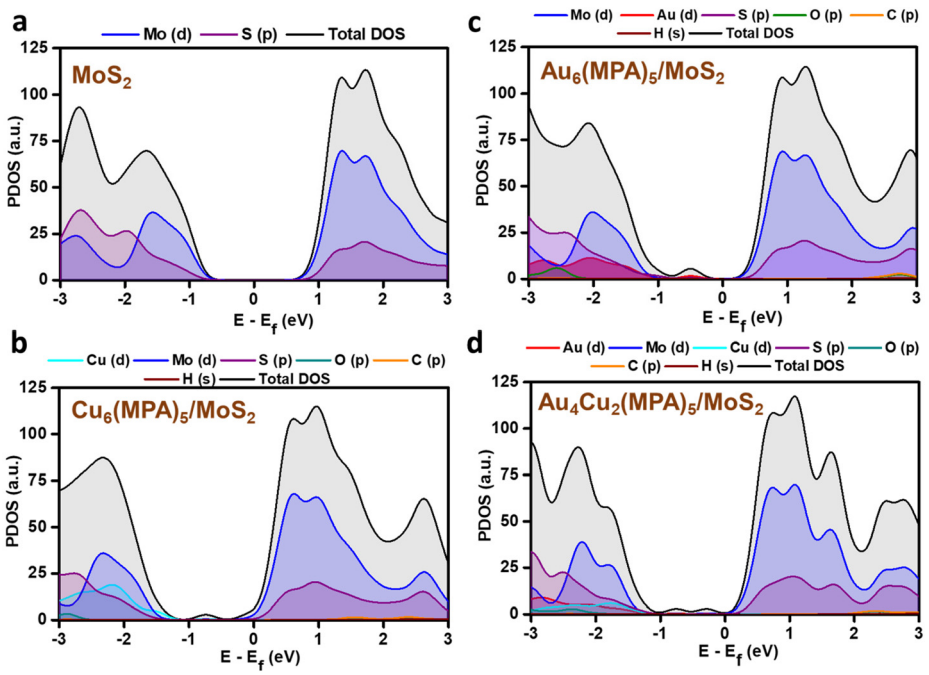

Fig. 7 Partial density of states (PDOS) of (a) pristine MoS_2, (b) $Cu_6(MPA)_5/MoS_2$, (c) $Au_6(MPA)_5/MoS_2$, and (d) $Au_4Cu_2(MPA)_5/MoS_2$ before H adsorption.

$Au_4Cu_2(MPA)_5/MoS_2$ catalyst. For the HER, an ideal catalyst would exhibit a nearly zero Gibbs free energy change (ΔG).[71] Calculated ΔG values for all the considered catalysts are shown in Fig. 5b. $Au_4Cu_2(MPA)_5/MoS_2$ with a ΔG value of −0.19 eV is calculated to be the most efficient catalyst for HER, followed by $Au_6(MPA)_5/MoS_2$ (−0.23 eV), $Cu_6(MPA)_5/MoS_2$ (−0.51 eV), and MoS_2 (1.54 eV), respectively. These findings are in excellent agreement with the experimental results. We further calculated the d-band center values for all the considered systems to understand their activity.[72,73] The calculated d-band center values of $Au_4Cu_2(MPA)_5/MoS_2$, $Au_6(MPA)_5/MoS_2$, $Cu_6(MPA)_5/MoS_2$, and MoS_2 with respect to the Fermi level (E_f) are −2.70, −1.81, −1.77, and −1.44 eV, respectively. These values illustrate that the $Au_4Cu_2(MPA)_5/MoS_2$ d-band center value is far from the E_f, followed by $Au_6(MPA)_5/MoS_2$, $Cu_6(MPA)_5/MoS_2$, and MoS_2, respectively. The closer (farther) the d-band center value is to E_f, the stronger (weaker) the H bonding with the metal. Therefore, the d-band center values of the clusters follow the same trend in HER activity: $Au_4Cu_2(MPA)_5/MoS_2$ > $Au_6(MPA)_5/MoS_2$ > $Cu_6(MPA)_5/MoS_2$ > MoS_2.

PDOS analysis of the H-adsorbed clusters (Fig. 6) reflects the interactions of H with different elements. The H states appear close to the Fermi level in the case of pure MoS_2 surface and there is strong overlap with the Mo/S states, which could be due to strong interaction with the pure MoS_2 surface. Similarly, the adsorbed H is found to be interacting with the Au/Cu, Au, and Cu states of $Au_4Cu_2(MPA)_5/MoS_2$, $Au_6(MPA)_5/MoS_2$, and $Cu_6(MPA)_5/MoS_2$ clusters, respectively. However, there is not much difference in the overlap between Au/Cu and H states in these clusters. Additionally, the $Au_6(MPA)_5/MoS_2$ and MoS_2 show metallic behavior after H adsorption. On the other hand, there is a shift in the valence band edge of $Au_6(MPA)_5/MoS_2$ and $Au_4Cu_2(MPA)_5/MoS_2$ in the presence of an H atom (Fig. 6 and 7). This suggests that there is a strong interaction between the H atom and clusters and that the transition is maximum for MoS_2, which is very much in agreement with the change in the Gibbs free energy.

Conclusions

In summary, Cu and Au are known to be poor HER catalysts, but here we found that combining them as bimetallic Au_4Cu_2 NCs over MoS_2 made the combination more effective for electrocatalytic water splitting in comparison to monometallic Au_6 NC and Cu_6 NC composites with MoS_2. The bimetallic Au_4Cu_2/MoS_2 composite exhibits excellent current density at minimal overpotential among the other considered catalysts. Moreover, Au_4Cu_2/MoS_2 shows a decrease in Tafel slope of 31 mV dec^{-1} and 4 times enhancement in C_{dl} in comparison to bare MoS_2, indicating strong electronic interaction between the Au_4Cu_2 NCs and the MoS_2 interface, as confirmed by XPS studies. Furthermore, due to the precisely structured Au_4Cu_2 NCs, theoretical calculations unveiled the better adsorption characteristics of H atoms in the Au_4Cu_2/MoS_2 catalyst, leading to enhanced HER performance. These results further corroborated the observed downshift in the d-band of the Au_4Cu_2/MoS_2 composite, directly impacting the binding energy of intermediate species. Hence, bimetallic nanoclusters are found to be promising for effective electrocatalytic water splitting in comparison to monometallic Au_6 NC and Cu_6 NC composites with MoS_2.

Author contributions

AD contributed to the investigation, methodology, data curation, and writing of the original draft. HM and AD performed computational analysis. LS helped in the conceptualization and editing of the draft. Rashi helped with data curation and reviewing the draft. SG and SM helped in ESI-mass analysis. BP contributed to computational analysis. AP contributed to the supervision, validation, project administration, and final review.

Conflicts of interest

There are no conflicts to declare.

Acknowledgements

SERB-DST is gratefully acknowledged for financial support. AD, Rashi, and L. S. acknowledge INST for doctoral fellowships and post-doctoral fellowships, respectively. We acknowledge IIT Indore for its laboratory and computational facilities. The work is supported by DST-SERB [Project No. CRG/2022/000836] and CSIR [Project No. 01(3046)/21/EMR-II]. H. M. thanks MHRD for PMRF and UGC for the research fellowship, respectively.

References

1 Z. W. Seh, J. Kibsgaard, C. F. Dickens, I. Chorkendorff, J. K. Nørskov and T. F. Jaramillo, *Science*, 2017, **355**, eaad4998.
2 P. Poizot and F. Dolhem, *Energy Environ. Sci.*, 2011, **4**, 2003–2019.
3 J. A. Turner, *Science*, 2004, **305**, 972–974.
4 K. Kwak, W. Choi, Q. Tang, M. Kim, Y. Lee, D.-e. Jiang and D. Lee, *Nat. Commun.*, 2017, **8**, 14723.
5 T. T. Yang, T. L. Tan and W. A. Saidi, *Chem. Mater*, 2020, **32**, 1315–1321.
6 T. Zeng, X. Meng, H. Huang, L. Zheng, H. Chen, Y. Zhang, W. Yuan and L. Y. Zhang, *Small*, 2022, **18**, e2107623.
7 S. L. Zhang, X. F. Lu, Z.-P. Wu, D. Luan and X. W. Lou, *Angew. Chem., Int. Ed.*, 2021, **60**, 19068–19073.
8 W. Cheng, H. Zhang, D. Luan and X. W. Lou, *Sci. Adv.*, 2021, **7**, eabg2580.

9 L. Zeng, Z. Zhao, Q. Huang, C. Zhou, W. Chen, K. Wang, M. Li, F. Lin, H. Luo, Y. Gu, L. Li, S. Zhang, F. Lv, G. Lu, M. Luo and S. Guo, *J. Am. Chem. Soc.*, 2023, **145**, 21432–21441.
10 X.-K. Wan, H. B. Wu, B. Y. Guan, D. Luan and X. W. Lou, *Adv. Mater.*, 2020, **32**, 1901349.
11 J. W. Park, G. Park, M. Kim, M. Han, J. Jang, Y. Yamauchi, B. Yuliarto, P. Krüger, J. Kim, N. Park and H. Lim, *Chem. Eng. J.*, 2023, **468**, 143733.
12 H. Lim, K. Kani, J. Henzie, T. Nagaura, A. S. Nugraha, M. Iqbal, Y. S. Ok, M. S. A. Hossain, Y. Bando, K. C. W. Wu, H.-J. Kim, A. E. Rowan, J. Na and Y. Yamauchi, *Nat. Protoc.*, 2020, **15**, 2980–3008.
13 H. Lim, J. Kim, K. Kani, M. K. Masud, H. Park, M. Kim, S. M. Alsheri, T. Ahamad, N. Alhokbany, J. Na, V. Malgras, Y. Bando and Y. Yamauchi, *Small*, 2020, **16**, 1902934.
14 Q. Lu, G. S. Hutchings, W. Yu, Y. Zhou, R. V. Forest, R. Tao, J. Rosen, B. T. Yonemoto, Z. Cao, H. Zheng, J. Q. Xiao, F. Jiao and J. G. Chen, *Nat. Commun.*, 2015, **6**, 6567.
15 W. Li, X. Wang, D. Xiong and L. Liu, *Int. J. Hydrogen Energy*, 2016, **41**, 9344–9354.
16 D. Voiry, M. Salehi, R. Silva, T. Fujita, M. Chen, T. Asefa, V. B. Shenoy, G. Eda and M. Chhowalla, *Nano Lett.*, 2013, **13**, 6222–6227.
17 J. Kibsgaard, Z. Chen, B. N. Reinecke and T. F. Jaramillo, *Nat. Mater.*, 2012, **11**, 963–969.
18 W. Jaegermann and H. Tributsch, *Prog. Surf. Sci.*, 1988, **29**, 1–167.
19 C. Tsai, K. Chan, J. K. Nørskov and F. Abild-Pedersen, *Science*, 2015, **640**, 133–140.
20 E. P. C. Higgins, A. A. Papaderakis, C. Byrne, R. Cai, A. Elgendy, S. J. Haigh, A. S. Walton, D. J. Lewis and R. A. W. Dryfe, *J. Phys. Chem. C*, 2021, **125**, 20940–20951.
21 J. Wang, W. Fang, Y. Hu, Y. Zhang, J. Dang, Y. Wu, H. Zhao and Z. Li, *Catal. Sci. Technol.*, 2020, **10**, 154–163.
22 Y. Li, S. Wang, Y. Hu, X. Zhou, M. Zhang, X. Jia, Y. Yang, B.-L. Lin and G. Chen, *J. Mater. Chem. A*, 2022, **10**, 5273–5279.
23 I. Chakraborty and T. Pradeep, *Chem. Rev.*, 2017, **117**, 8208–8271.
24 J. Choi, S. Seo, M. Kim, Y. Han, X. Shao and H. Lee, *Small*, 2023, 2304560.
25 H. Yan, H. Xiang, J. Liu, R. Cheng, Y. Ye, Y. Han and C. Yao, *Small*, 2022, **18**, 2200812.
26 S. Mondal, S. Dutta, S. Mal, S. K. Pati and S. Bhattacharyya, *Angew. Chem., Int. Ed.*, 2023, **62**, e202301269.
27 J. Ding, H. Yang, S. Zhang, Q. Liu, H. Cao, J. Luo and X. Liu, *Small*, 2022, **18**, 2204524.
28 Y. Du, H. Sheng, D. Astruc and M. Zhu, *Chem. Rev.*, 2020, **120**, 526–622.
29 X. Kang and M. Zhu, *Chem. Soc. Rev.*, 2019, **48**, 2422–2457.
30 R. Jin, C. Zeng, M. Zhou and Y. Chen, *Chem. Rev.*, 2016, **116**, 10346–10413.
31 Rashi, D. Bain, A. Devi, S. Chakraborty and A. Patra, *ACS Sustainable Chem. Eng.*, 2023, **11**, 1995–2004.
32 D. Bain, A. Devi, Rashi, S. Chakraborty, S. Kolay and A. Patra, *J. Phys. Chem. C*, 2023, **127**, 18244–18251.
33 L. Sahoo, A. Devi and A. Patra, *ACS Sustainable Chem. Eng.*, 2023, **11**, 4187–4196.
34 M. Ghosal Chowdhury, L. Sahoo, S. Maity, D. Bain, U. K. Gautam and A. Patra, *ACS Appl. Nano Mater.*, 2022, **5**, 7132–7141.
35 Z. Cui, W. Jiao, Z. Huang, G. Chen, B. Zhang, Y. Han and W. Huang, *Small*, 2023, **19**, 2301465.
36 T. Gao, X. Tang, X. Li, S. Wu, S. Yu, P. Li, D. Xiao and Z. Jin, *ACS Catal.*, 2023, **13**, 49–59.
37 T. Kawawaki and Y. Negishi, *Nanomaterials*, 2020, **10**, 238.
38 Q. Zhu, X. Huang, Y. Zeng, K. Sun, L. Zhou, Y. Liu, L. Luo, S. Tian and X. Sun, *Nanoscale Adv.*, 2021, **3**, 6330–6341.
39 X. Li, S. Takano and T. Tsukuda, *J. Phys. Chem. C*, 2021, **125**, 23226–23230.
40 S. Zhao, R. Jin, H. Abroshan, C. Zeng, H. Zhang, S. D. House, E. Gottlieb, H. J. Kim, J. C. Yang and R. Jin, *J. Am. Chem. Soc.*, 2017, **139**, 1077–1080.
41 H. Mousavi, Y. Yin, S. K. Sharma, C. T. Gibson, V. Golovko, G. G. Andersson, C. J. Shearer and G. F. Metha, *J. Phys. Chem. C*, 2022, **126**, 246–260.
42 S. Zhao, R. Jin, Y. Song, H. Zhang, S. D. House, J. C. Yang and R. Jin, *Small*, 2017, **13**, 1701519.
43 S. Gratious, A. Karmakar, D. Kumar, S. Kundu, S. Chakraborty and S. Mandal, *Nanoscale*, 2022, **14**, 7919–7926.
44 X. Kang, Y. Li, M. Zhu and R. Jin, *Chem. Soc. Rev.*, 2020, **49**, 6443–6514.
45 Y. Du, J. Xiang, K. Ni, Y. Yun, G. Sun, X. Yuan, H. Sheng, Y. Zhu and M. Zhu, *Inorg. Chem. Front.*, 2018, **5**, 2948–2954.
46 W. Choi, G. Hu, K. Kwak, M. Kim, D.-e. Jiang, J.-P. Choi and D. Lee, *ACS Appl. Mater. Interfaces*, 2018, **10**, 44645–44653.
47 Y. Tang, F. Sun, X. Ma, L. Qin, G. Ma, Q. Tang and Z. Tang, *Dalton Trans.*, 2022, **51**, 7845–7850.
48 J. Zhang, Y. Liu, C. Sun, P. Xi, S. Peng, D. Gao and D. Xue, *ACS Energy Lett.*, 2018, **3**, 779–786.
49 W. Li, D. Xiong, X. Gao, W.-G. Song, F. Xia and L. Liu, *Catal. Today*, 2017, **287**, 122–129.
50 G. Kresse and D. Joubert, *Phys. Rev. B: Condens. Matter Mater. Phys.*, 1999, **59**, 1758–1775.
51 P. E. Blöchl, *Phys. Rev. B: Condens. Matter Mater. Phys.*, 1994, **50**, 17953–17979.
52 J. P. Perdew, K. Burke and M. Ernzerhof, *Phys. Rev. Lett.*, 1996, **77**, 3865–3868.
53 J. Greeley, T. F. Jaramillo, J. Bonde, I. Chorkendorff and J. K. Nørskov, *Nat. Mater.*, 2006, **5**, 909–913.
54 J. K. Nørskov, T. Bligaard, A. Logadottir, J. R. Kitchin, J. G. Chen, S. Pandelov and U. Stimming, *J. Electrochem. Soc.*, 2005, **152**, J23.
55 J. K. Nørskov, J. Rossmeisl, A. Logadottir, L. Lindqvist, J. R. Kitchin, T. Bligaard and H. Jónsson, *J. Phys. Chem. B*, 2004, **108**, 17886–17892.
56 A. Devi, H. Seksaria, D. Bain, S. Kolay, Rashi, A. De Sarkar and A. Patra, *Phys. Chem. Chem. Phys.*, 2023, **25**, 9513–9521.

57 C. Comby-Zerbino, X. Dagany, F. Chirot, P. Dugourd and R. Antoine, *Mater. Adv.*, 2021, **2**, 4896–4913.
58 E. C. Dreaden, A. M. Alkilany, X. Huang, C. J. Murphy and M. A. El-Sayed, *Chem. Soc. Rev.*, 2012, **41**, 2740–2779.
59 S. Maity, D. Bain and A. Patra, *J. Phys. Chem. C*, 2019, **123**, 2506–2515.
60 R. Gusain, N. Kumar, F. Opoku, P. P. Govender and S. S. Ray, *ACS Appl. Nano Mater.*, 2021, **4**, 4721–4734.
61 D. M. Chevrier, M. A. MacDonald, A. Chatt, P. Zhang, Z. Wu and R. Jin, *J. Phys. Chem. C*, 2012, **116**, 26947–26947.
62 D. Bain, S. Maity, B. Paramanik and A. Patra, *ACS Sustainable Chem. Eng.*, 2018, **6**, 2334–2343.
63 X. Gao, Y. Lu, M. Liu, S. He and W. Chen, *J. Mater. Chem. C*, 2015, **3**, 4050–4056.
64 L. Liang and V. Meunier, *Nanoscale*, 2014, **6**, 5394–5401.
65 W. Zhou, M. Chen, M. Guo, A. Hong, T. Yu, X. Luo, C. Yuan, W. Lei and S. Wang, *Nano Lett.*, 2020, **20**, 2923–2930.
66 V. K. Singh, U. Gupta, B. Mukherjee, S. Chattopadhyay and S. Das, *ACS Appl. Nano Mater.*, 2021, **4**, 886–896.
67 A. Mondal, H. R. Inta, A. Roy, A. Kumar Mahato and V. Mahalingam, *ACS Appl. Nano Mater.*, 2023, **6**, 12040–12049.
68 J. Jin, J. Yin, H. Liu, B. Huang, Y. Hu, H. Zhang, M. Sun, Y. Peng, P. Xi and C.-H. Yan, *Angew. Chem., Int. Ed.*, 2021, **60**, 14117–14123.
69 L. Sahoo, S. Mondal, C. B. Nayana and U. K. Gautam, *J. Colloid Interface Sci.*, 2021, **590**, 175–185.
70 A. Posada-Amarillas, R. Pacheco-Contreras, S. Morales-Meza, M. Sánchez and J. C. Schön, *Int. J. Quantum Chem.*, 2016, **116**, 1006–1015.
71 N. K. Pandit, D. Roy, S. C. Mandal and B. Pathak, *J. Phys. Chem. Lett.*, 2022, **13**, 7583–7593.
72 H. Xin, A. Vojvodic, J. Voss, J. K. Nørskov and F. Abild-Pedersen, *Phys. Rev. B: Condens. Matter Mater. Phys.*, 2014, **89**, 115114.
73 Z. Chen, Y. Song, J. Cai, X. Zheng, D. Han, Y. Wu, Y. Zang, S. Niu, Y. Liu, J. Zhu, X. Liu and G. Wang, *Angew. Chem., Int. Ed.*, 2018, **57**, 5076–5080.